

Citation for published version:

Troja, E, Lipunov, VM, Mundell, CG, Butler, RN, Watson, AM, Kobayashi, S, Cenko, SB, Marshall, FE, Ricci, R, Fruchter, AS, Wieringa, MH, Gorbovskoy, ES, Kornilov, V, Kutyrev, A, Lee, WH, Toy, V, Tyurina, NV, Budnev, NM, Buckley, DAH, González, J, Gress, O, Horesh, A, Panasyuk, MI, Prochaska, JX, Ramirez-ruiz, E, Lopez, RR, Richer, MG, Román-zúñiga, CG, Serra-Ricart, M, Yurkov, V & Gehrels, N 2017, 'Significant and variable linear polarization during the prompt optical flash of GRB 160625B', *Nature*, vol. 547, no. 7664, pp. 425-427. <https://doi.org/10.1038/nature23289>

DOI:

[10.1038/nature23289](https://doi.org/10.1038/nature23289)

Publication date:

2017

Document Version

Peer reviewed version

[Link to publication](#)

This is the Author Accepted Manuscript of an article published in final form in and available online via:
<https://doi.org/10.1038/nature23289>

University of Bath

Alternative formats

If you require this document in an alternative format, please contact:
openaccess@bath.ac.uk

General rights

Copyright and moral rights for the publications made accessible in the public portal are retained by the authors and/or other copyright owners and it is a condition of accessing publications that users recognise and abide by the legal requirements associated with these rights.

Take down policy

If you believe that this document breaches copyright please contact us providing details, and we will remove access to the work immediately and investigate your claim.

1 **Significant and variable linear polarization during a bright prompt**

2 **optical flash**

3 E. Troja^{1,2}, V. M. Lipunov^{3,4}, C. G. Mundell⁵, N. R. Butler⁶, A. M. Watson⁷, S. Kobayashi⁸, S. B.
4 Cenko^{2,1}, F. E. Marshall², R. Ricci⁹, A. Fruchter¹⁰, M. H. Wieringa¹¹, E. S. Gorbovskoy^{3,4}, V.
5 Kornilov^{3,4}, A. Kuttyrev^{1,2}, W. H. Lee⁷, V. Toy¹, N. V. Tyurina^{3,4}, N. M. Budnev¹², D. A. H.
6 Buckley¹³, J. González⁷, O. Gress¹², A. Horesh¹⁴, M. I. Panasyuk¹⁵, J. X. Prochaska¹⁶, E.
7 Ramirez- Ruiz¹⁶, R. Rebolo Lopez¹⁷, M. G. Richer¹⁸, C. Román-Zúñiga¹⁸, M. Serra-Ricart¹⁷, V.
8 Yurkov¹⁹, and N. Gehrels²

9 ¹Department of Astronomy, University of Maryland, College Park, MD 20742-4111, USA

10 ²NASA Goddard Space Flight Center, 8800 Greenbelt Rd, Greenbelt, MD 20771, USA

11 ³M.V. Lomonosov Moscow State University, Physics Department, Leninskie Gory, GSP-1,
12 Moscow 119991, Russia⁴

13 ⁴M.V. Lomonosov Moscow State University, Sternberg Astronomical Institute, Universitetsky
14 pr., 13, Moscow 119234, Russia

15 ⁵Department of Physics, University of Bath, Claverton Down, Bath, BA2 7AY, UK

16 ⁶School of Earth & Space Exploration, Arizona State University, AZ 85287, USA⁷

17 ⁷Instituto de Astronomía, Universidad Nacional Autónoma de México, Apartado Postal 70-264,
18 04510 Cd. de México, México⁸

19 ⁸Astrophysics Research Institute, Liverpool John Moores University, IC2 Building, Liverpool
20 Science Park, 146 Brownlow Hill, Liverpool L3 5RF, United Kingdom⁹

21 ⁹INAF-Istituto di Radioastronomia, Via Gobetti 101, I-40129 Bologna, ITALY¹⁰

22 ¹⁰Space Telescope Science Institute, 3700 San Martin Drive, Baltimore, MD 21218, USA

23 ¹¹CSIRO Astronomy and Space Science, PO Box 76, Epping NSW 1710, Australia^[SEP]

24 ¹²Irkutsk State University, Applied Physics Institute, 20, Gagarin Blvd, 664003 Irkutsk, Russia

25 ¹³South African Astronomical Observatory, PO Box 9, 7935 Observatory, Cape Town, South

26 Africa^[SEP]

27 ¹⁴Racah Institute of Physics, Hebrew University, Jerusalem, 91904, Israel^[SEP]

28 ¹⁵Skobeltsyn Institute of Nuclear Physics of Lomonosov, Moscow State University, Vorob'evy

29 Gory, 119991 Moscow, Russia

30 ¹⁶University of California Observatories, 1156 High St., Santa Cruz, CA 95064 USA^[SEP]

31 ¹⁷Instituto de Astrofísica de Canarias Via Lactea, s/n E38205, La Laguna (Tenerife), Spain

32 ¹⁸Instituto de Astronomía, Universidad Nacional Autónoma de México, Apartado Postal 106,

33 22800 Ensenada, Baja California, México^[SEP]

34 ¹⁹Blagoveschensk State Pedagogical University, Lenin str., 104, Amur Region, Blagoveschensk

35 675000, Russia

36

37 **Measurement of polarized light provides a direct probe of magnetic fields in collimated**

38 **outflows (jets) of relativistic plasma from accreting stellar-mass black holes at cosmological**

39 **distances. These outflows power brief and intense flashes of prompt gamma-rays known as**

40 **Gamma Ray Bursts (GRBs), followed by longer-lived afterglow radiation detected across**

41 **the electromagnetic spectrum. Rapid-response polarimetric observations of newly**

42 **discovered GRBs have probed the initial afterglow phase¹⁻³. Linear polarization degrees as**

43 **high as $\Pi \sim 30\%$ are detected minutes after the end of the prompt GRB emission, consistent**

44 **with a stable, globally ordered magnetic field permeating the jet at large distances from the**

45 **central source³. In contrast, optical⁴⁻⁶ and gamma-ray⁷⁻⁹ observations during the prompt**

46 phase led to discordant and often controversial¹⁰⁻¹² results, and no definitive conclusions
47 on the origin of the prompt radiation or the configuration of the magnetic field could be
48 derived. Here we report the detection of linear polarization of a prompt optical flash that
49 accompanied the extremely energetic and long-lived prompt gamma-ray emission from
50 GRB 160625B. Our measurements probe the structure of the magnetic field at an early
51 stage of the GRB jet, closer to the central source, and show that the prompt GRB phase is
52 produced via fast cooling synchrotron radiation in a large-scale magnetic field advected
53 from the central black hole and distorted from dissipation processes within the jet.

54 On 25 June 2016 at 22:40:16.28 Universal Time (UT), the Gamma-Ray Burst Monitor (GBM)
55 aboard NASA's *Fermi* Gamma-ray Space Telescope discovered GRB 160625B as a short-lived
56 (~ 1 s) pulse of γ -ray radiation (G1 in Fig. 1). An automatic localization was rapidly distributed
57 by the spacecraft allowing wide-field optical facilities to start follow-up observations. Three
58 minutes after the first alert, at 22:43:24.82 UT (hereafter T_0), the Large Area Telescope (LAT)
59 aboard *Fermi* triggered on another bright and longer lasting (~ 30 s) pulse (G2 in Fig. 1) visible
60 up to GeV energies¹³. A rapid increase in brightness was simultaneously observed at optical
61 wavelengths (Fig. 1). The optical light rose by a factor of 100 in a few seconds reaching its peak
62 at $T_0+5.9$ s with an observed visual magnitude of 7.9. After a second fainter peak at $T_0+15.9$ s,
63 the optical light is seen to steadily decline. During this phase the MASTER¹⁴-IAC telescope
64 simultaneously observed the optical counterpart in two orthogonal polaroids starting at T_0+95 s
65 and ending at T_0+360 s. A detection of a polarized signal with this instrumental configuration
66 provides a lower bound to the true degree of linear polarization, $\Pi_{L,\min} = (I_2 - I_1) / (I_1 + I_2)$ where
67 I_1 and I_2 refer to the source intensity in each filter. Significant levels of linear polarization of up
68 to $\Pi_{L,\min} = 8.0 \pm 0.5\%$ were detected compared with values $< 2\%$ for other nearby objects with

69 similar brightness (Fig. 2). Over this time interval a weak tail of gamma-ray emission is visible
70 until the onset of a third longer lived episode of prompt gamma-ray radiation (G3), starting at
71 T_0+337 s and ending at T_0+630 s.

72 In the standard GRB model^{15,16}, after the jet is launched dissipation processes within the ultra-
73 relativistic flow produce a prompt flash of radiation, mostly visible in gamma-rays. Later, the jet
74 outermost layers interact with the surrounding medium and two shocks develop, one propagating
75 outward into the external medium (forward shock) and the other one traveling backward into the
76 jet (reverse shock). These shocks heat up the ambient electrons, which emit, via synchrotron
77 emission, a broadband afterglow radiation. At very early time ($\sim T_0+10$ s) the observed optical
78 flux from GRB 160625B is orders of magnitude brighter than the extrapolated prompt emission
79 component (Fig. 3), suggesting that optical and gamma-ray emission originate from different
80 physical locations in the flow. A plausible interpretation is that the early ($\sim T_0+10$ s) optical
81 emission arises from a strong reverse shock, although internal dissipation processes are also
82 possible (see Methods). A general prediction of the reverse shock model¹⁷ is that, after reaching
83 its peak, the optical flash should decay as a smooth power-law with slope of -2. However, in our
84 case, the optical light curve is more complex: its temporal decay is described by a series of
85 power-law segments with slopes between -0.3 and -1.8. The shallower decay could be in part
86 explained by the ejection of a range of Lorentz factors, as the blastwave is refreshed by the
87 arrival of the slower moving ejecta¹⁸. However, this would require ad-hoc choices of the Lorentz
88 factor distribution in order to explain each different power-law segment and does not account for
89 the observed temporal evolution of the polarization. Our observations are more naturally
90 explained by including a second component of emission in the optical range, which dominates
91 for $T > T_0+300$ s. Our broadband spectral analysis (see Methods) rules out a significant

92 contribution from the forward shock, whose emission is negligible at this time ($f_{\text{FS}} < 1$ mJy).
93 Instead, the prompt optical component makes a substantial contribution ($>40\%$) to the observed
94 optical light (Fig. 3).

95 The only other case of a time-resolved polarimetric study³ showed that the properties of the
96 reverse shock remain roughly constant in time. Our measurements hint at a different temporal
97 trend. The fractional polarization appears stable over the first three exposures, and changes with
98 high significance ($\approx 99.9996\%$) in the last temporal bin (Fig. 2). Based on our broadband dataset
99 we can confidently rule out geometric effects as the cause of the observed change. If the
100 observer's line of sight intercepts the jet edges, it would cause a steeper decay of the optical flux
101 and is also not consistent with the detection of an achromatic jet-break at much later times
102 (Extended Data Figure 1). The temporal correlation between the gamma-ray flux and the
103 fractional polarization (Fig. 2) and the significant contribution of the prompt component to the
104 optical emission (Fig. 3) suggest that the gamma-ray and optical photons are co-located and that
105 the observed variation in $\Pi_{\text{L,min}}$ is connected to the renewed jet activity. Thus our last observation
106 detected the linear optical polarization of the prompt emission, directly probing the jet properties
107 at the smaller radius from where prompt optical and gamma-ray emissions originate.

108 Three main emission mechanisms are commonly invoked to explain the prompt GRB phase, and
109 all three of them can in principle lead to a significant level of polarization. Inverse Compton (IC)
110 scattering and photospheric emission could lead to non-zero polarization only if the spherical
111 symmetry of the emitting patch is broken by the jet edges. However, as explained above, an off-
112 axis model is not consistent with our dataset. Furthermore, an IC origin of the observed prompt
113 phase would imply a prominent high-energy (>1 GeV) component, in contrast with the
114 observations¹⁹. The most plausible source of the observed photons is synchrotron radiation from

115 a population of fast cooling electrons moving in strong magnetic fields. This can account for the
116 low-energy spectral slope $\alpha \sim -1.5$ (see Methods) and the high degree of polarization. An
117 analogous conclusion, based on different observational evidence, was reached by an independent
118 work on this burst¹⁹.

119 If the magnetic field is produced by local instabilities in the shock front, the polarized radiation
120 would come from a number of independent patches with different field orientations. This model
121 does not reproduce well our data. It predicts erratic fluctuations of the polarization angle and a
122 maximum level of polarization^{20,21} $\Pi_{\text{MAX}} \approx \Pi_{\text{syn}} / \sqrt{N} \approx 2\text{-}3\%$ where $\Pi_{\text{syn}} \sim 70\%$ is the intrinsic
123 polarization of the synchrotron radiation²², and $N \approx 1,000$ is the number of magnetic patches²³.
124 Our observations are instead easily accommodated by a large-scale magnetic field advected from
125 the central source. Recent claims of a variable polarization angle during the prompt γ -ray
126 emission hinted, although not unambiguously, at a similar configuration⁹.

127 This model^{21,24} can explain the stable polarization measurements, the high degree of polarization,
128 and its rapid change simultaneous with the onset of the new prompt episode. In this model the
129 magnetic field is predominantly toroidal, and the polarization angle is constant. If relativistic
130 aberration is taken into account²⁴, the polarization degree can be as high as $\approx 50\%$. In this case
131 the probability of measuring a polarization as low as $\Pi_{\text{L,min}} \sim 8\%$ is approximately 10% (see
132 Methods). It appears more likely that the actual polarization degree is lower than the maximum
133 possible value and closer to our measurement, suggesting that the large-scale magnetic field
134 might be significantly distorted by internal collisions^{25,26} or kink instabilities²⁷ at smaller radii
135 before the reconnection process produces bright gamma-rays.

136 Our results suggest that GRB outflows might be launched as Poynting flux dominated jets whose
137 magnetic energy is rapidly dissipated close to the source, after which they propagate as hot


138 baryonic jets with a relic magnetic field. A large-scale magnetic field is therefore a generic
139 property of GRB jets and the production of a bright optical flash depends on how jet instabilities
140 develop near the source and their efficiency in magnetic suppression. The dissipation of the
141 primordial magnetic field at the internal radius, as observed for GRB 160625B, is critical for the
142 efficient acceleration of particles to the highest ($>10^{20}$ eV) energies^{25,28}. However, the ordered
143 superluminal component at the origin of the observed polarization and the relatively high
144 magnetization ($\sigma\sim 0.1$; see Methods) of the ejecta might hinder particle acceleration through
145 shocks²⁸, thus suggesting that either GRBs are not sources of ultra high-energy cosmic-rays as
146 bright as previously thought or that other acceleration mechanisms²⁹ need to be considered.

147

- 148 1. Mundell, C. G., Steele, I. A., Smith, R. J., et al. Early Optical Polarization of a Gamma- Ray
149 Burst Afterglow. *Science* **315**, 1822-1824 [SEP](2007)
- 150 2. Steele, I. A., Mundell, C. G., Smith, R. J., Kobayashi, S., & Guidorzi, C. Ten per cent
151 polarized optical emission from GRB090102. *Nature* **462**, 767-769 [SEP](2009)
- 152 3. Mundell, C. G., Kopač, D., Arnold, D. M., et al. Highly polarized light from stable ordered
153 magnetic fields in GRB 120308A. *Nature* **504**, 119-121 (2013)[SEP]
- 154 4. Kopač, D., Mundell, C. G., Japelj, J., et al. Limits on Optical Polarization during the Prompt
155 Phase of GRB 140430A. *Astrophys. J.* **813**, 1 (2015)
- 156 5. Pruzhinskaya, M. V., Krushinsky, V. V., Lipunova, G. V., et al. Optical polarization
157 observations with the MASTER robotic net. *New Astronomy* **29**, 65-74 [SEP](2014)
- 158 6. Gorbovskoy, E. S., Lipunov, V. M., Buckley, D. A. H., et al. Early polarization observations
159 of the optical emission of gamma-ray bursts: GRB 150301B and GRB 150413A. *Mon. Not.*
160 *R. Astron. Soc.* **455**, 3312-3318 [SEP](2016)

- 161 7. Coburn, W., & Boggs, S. E. Polarization of the prompt γ -ray emission from the γ -ray burst of
162 6 December 2002. *Nature* **423**, 415-417 [SEP](2003)
- 163 8. Götz, D., Laurent, P., Lebrun, F., Daigne, F., & Bošnjak, Ž. Variable Polarization Measured
164 in the Prompt Emission of GRB 041219A Using IBIS on Board INTEGRAL. *Astrophys. J.*
165 **695**, L208-L212 [SEP](2009)
- 166 9. Yonetoku, D., Murakami, T., Gunji, S., et al. Magnetic Structures in Gamma-Ray Burst Jets
167 Probed by Gamma-Ray Polarization. *Astrophys. J.* **758**, L1 [SEP](2012)
- 168 10. Rutledge, R. E., & Fox, D. B. Re-analysis of polarization in the γ -ray flux of GRB 021206.
169 *Mon. Not. R. Astron. Soc.* **350**, 1288-1300 [SEP](2004)
- 170 11. McGlynn, S., Clark, D. J., Dean, A. J., et al. Polarization studies of the prompt gamma-ray
171 emission from GRB 041219a using the spectrometer aboard INTEGRAL. *Astron. Astrophys.*
172 **466**, 895-904 (2007)
- 173 12. Kalemci, E., Boggs, S. E., Kouveliotou, C., Finger, M., & Baring, M. G. Search for
174 Polarization from the Prompt Gamma-Ray Emission of GRB 041219a with SPI on
175 INTEGRAL. *Astrophys. J. Supp.* **169**, 75-82 (2007)
- 176 13. Dirirsa, F., GRB 160625B: Fermi-LAT detection of a bright burst. *GCN Circ.* 19580 (2016)
- 177 14. Lipunov, V., Kornilov, V., Gorbovskoy, E., et al. Master Robotic Net. *Advances in*
178 *Astronomy* **2010**, 349171 [SEP](2010)
- 179 15. Piran, T. Gamma-ray bursts and the fireball model. *Physics Reports* **314**, 575-667 [SEP](1999)
- 180 16. Kumar, P., & Zhang, B. The physics of gamma-ray bursts relativistic jets. *Physics Reports*
181 [SEP]**561**, 1-109 [SEP](2015)
- 182 17. Kobayashi, S. Light Curves of Gamma-Ray Burst Optical Flashes. *Astrophys. J.* **545**, 807-
183 812 [SEP](2000)

- 184 18. Sari, R., & Mészáros, P. Impulsive and Varying Injection in Gamma-Ray Burst Afterglows.
185 *Astrophys. J.* **535**, L33-L37 (2000)
- 186 19. Zhang, B.-B., Zhang, B., Castro-Tirado, A. J., et al. Transition from Fireball to Poynting-
187 flux-dominated Outflow in Three-Episode GRB 160625B. Preprint at
188 <https://arxiv.org/abs/1612.03089> (2016)
- 189 20. Gruzinov, A., & Waxman, E. Gamma-Ray Burst Afterglow: Polarization and Analytic
190 ^[SEP]Light Curves. *Astrophys. J.* **511**, 852-861 ^[SEP](1999)
- 191 21. Granot, J., & Königl, A. Linear Polarization in Gamma-Ray Bursts: The Case for an
192 ^[SEP]Ordered Magnetic Field. *Astrophys. J.* **594**, L83-L87 ^[SEP](2003)
- 193 22. Rybicki, G. B., & Lightman, A. P. Radiative Processes in Astrophysics. Wiley-Interscience,
194 New York (1979)
- 195 23. Inoue, T., Asano, K., & Ioka, K. Three-dimensional Simulations of Magnetohydrodynamic
196 Turbulence Behind Relativistic Shock Waves and Their Implications for Gamma-Ray Bursts.
197 *Astrophys. J.* **734**, 77 ^[SEP](2011)
- 198 24. Lyutikov, M., Pariev, V. I., & Blandford, R. D. Polarization of Prompt Gamma-Ray Burst
199 Emission: Evidence for Electromagnetically Dominated Outflow. *Astrophys. J.* **597**, 998-
200 1009 (2003)
- 201 25. Zhang, B., & Yan, H. The Internal-collision-induced Magnetic Reconnection and Turbulence
202 (ICMART) Model of Gamma-ray Bursts. *Astrophys. J.* **726**, 90 ^[SEP](2011)
- 203 26. Deng, W., Zhang, H., Zhang, B., & Li, H. Collision-induced Magnetic Reconnection ^[SEP]and a
204 Unified Interpretation of Polarization Properties of GRBs and Blazars. *Astrophys. J.* **821**, L12
205 (2016)

- 206 27. Bromberg, O., & Tchekhovskoy, A. Relativistic MHD simulations of core-collapse GRB
207 jets: 3D instabilities and magnetic dissipation. *Mon. Not. R. Astron. Soc.* **456**, 1739-1760
208  (2016)
- 209 28. Sironi, L., & Spitkovsky, A. Particle Acceleration in Relativistic Magnetized Collision-less
210 Electron-Ion Shocks. *Astrophys. J.* **726**, 75 (2011)
- 211 29. Giannios, D. UHECRs from magnetic reconnection in relativistic jets. *Mon. Not. R. Astron.*
212 *Soc.* **408**, L46-L50 (2010)

213

214

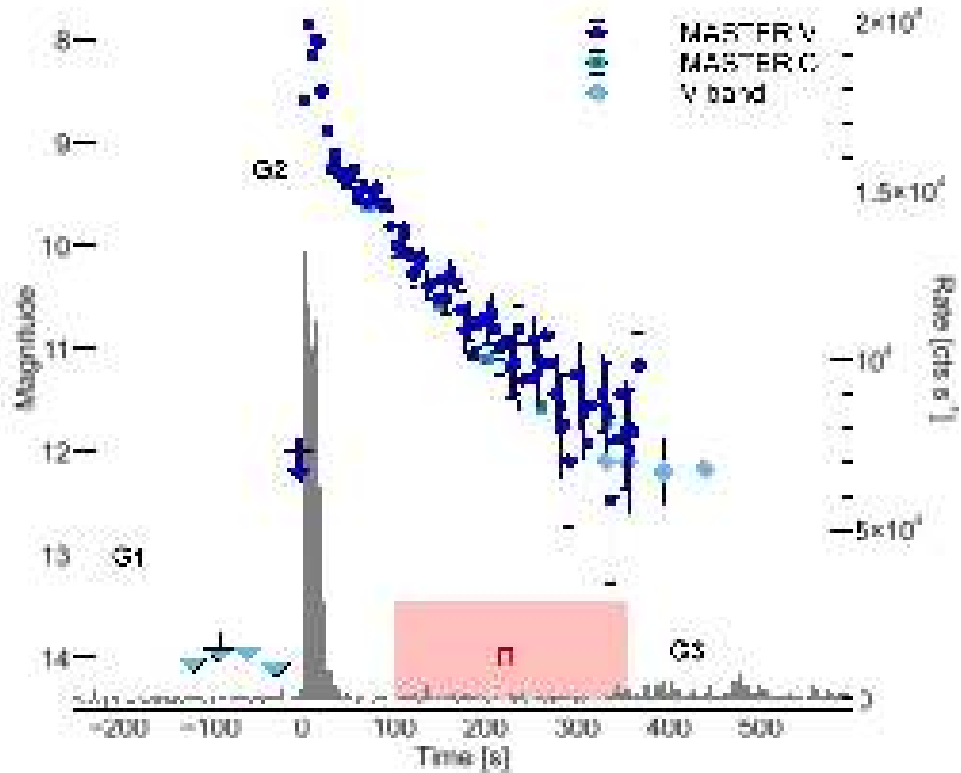
215

216

217

218

219



220

221 **Figure 1: Prompt gamma-ray and optical light curves of GRB160625B.**

222 The gamma-ray light curve (black; 10-250 keV) consists of three main episodes: a short
 223 precursor (G1), a bright main burst (G2), and a fainter and longer lasting tail of emission (G3).

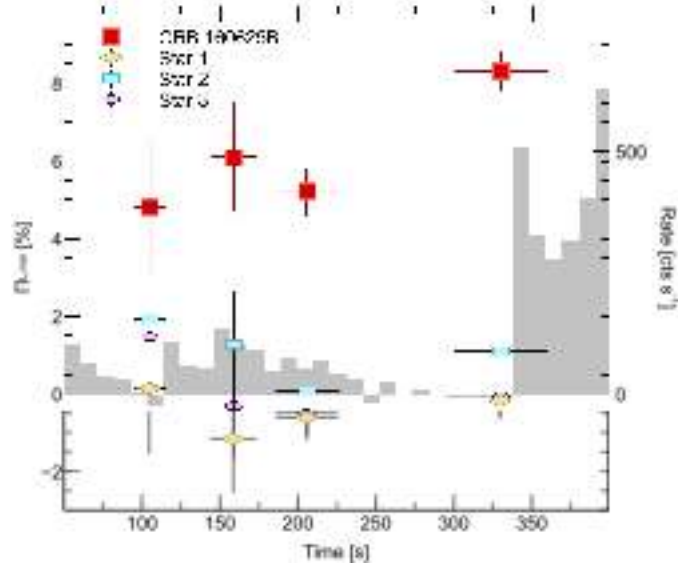
224 Optical data from the MASTER Net telescopes and other ground-based facilities¹⁹ are overlaid
 225 for comparison. Error bars are 1σ , upper limits are 3σ . The red box marks the time interval over
 226 which polarimetric measurements were carried out. Within the sample of nearly 2,000 bursts
 227 detected by the GBM, only 6 other events have a comparable duration. The majority of GRBs
 228 ends before the start of polarimetric observations.

229

230

231

232



233

234

235 **Figure 2: Temporal evolution of the optical polarization measured for GRB 160625B.**^{[1][SEP]}

236 The minimum polarization, measured in four different temporal bins (red squares), remains fairly
 237 constant over the first three exposures, then increases by 60% during the last observation. At the
 238 same time an evident increase in the gamma-ray count rates (gray shaded area; 5 s time bins)
 239 marks the onset of the third episode of prompt emission (G3). The spectral shape and fast
 240 temporal variability observed during G3 are typical of the GRB prompt emission. For
 241 comparison, we also report simultaneous polarimetric measurements of the three brightest stars
 242 in the MASTER-IAC field of view. Error bars are 1σ .

243

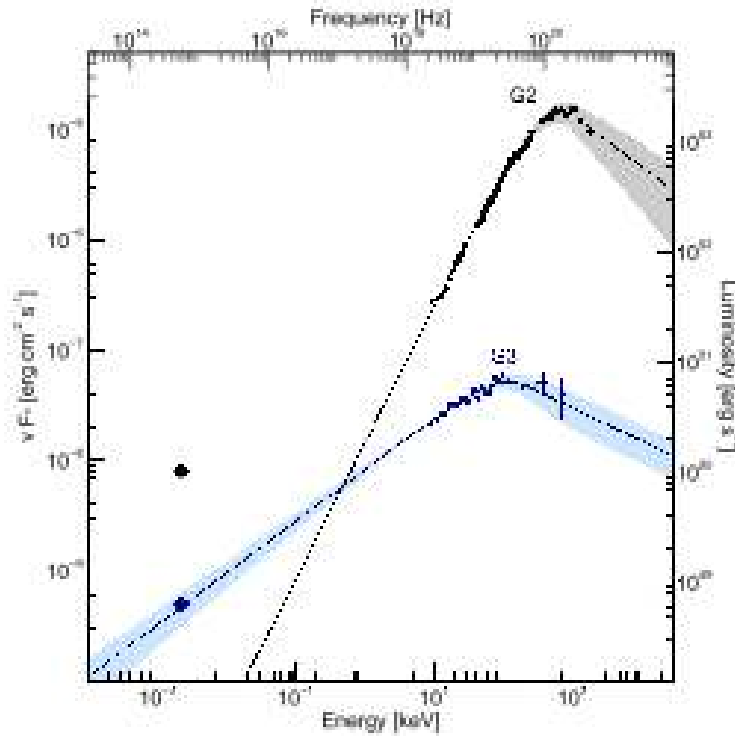
244

245

246

247

248



250

251

252 **Figure 3: Broadband spectra of the prompt phase in GRB 160625B.**

253 Spectra are shown for the two main episodes of prompt emission, labeled as G2 and G3. Error

254 bars are 1σ . The gamma-ray spectra were modeled with a smoothly broken power-law (solid

255 line). The 1σ uncertainty in the best fit model is shown by the shaded area. The diamonds

256 indicate the average optical flux (corrected for Galactic extinction) observed during the same

257 time intervals. The extrapolated contribution of the prompt gamma-ray component to the optical

258 band is non negligible during G3 and constitutes $>40\%$ of the observed emission.

259

260

261

262 **Methods**

263 **MASTER Observations**

264 The MASTER-IAC telescope, located at Teide Observatory (Tenerife, Spain), responded to the
265 first GBM alert and started observing the field with its very wide field camera at T_0-133 s.
266 Observations were performed with a constant integration time of 5 s and ended at T_0+350 s. The
267 MASTER II telescope responded to the LAT alert¹³ and observed the GRB position between
268 T_0+65 s and T_0+360 s. The resulting light curves are shown in Fig. 1. Polarimetric observations
269 started at T_0+95 s in response to the LAT trigger. However, due to a software glitch, they were
270 scheduled as a series of tiled exposures covering a larger area. This caused the telescope to slew
271 away from the burst true position at T_0+360 s. A total of four useful exposures were collected
272 (Extended Data Table 1). Data were reduced in a standard fashion^{5,14}. The two synchronous
273 frames used to measure the polarization were mutually calibrated so that the average polarization
274 for comparison stars is zero. This procedure removes the effects of interstellar polarization. The
275 significance of the polarimetric measurements was assessed through Monte Carlo simulations.
276 Extended Data Figure 2 shows the resulting distribution of polarization values and significances.

277 ***Swift* Observations**

278 *Swift* observations span the period from $T_0+9.6$ ks to T_0+48 days. XRT data were collected in
279 Photon Counting (PC) mode for a total net exposure of 134 ks. The optical afterglow was
280 monitored with the UVOT in the u , v , and wl filters for 10 days after the burst, after which it fell
281 below the UVOT detection threshold. Subsequent observations were performed using the UVOT
282 filter of the day. *Swift* data were processed using the *Swift* software package within HEASOFT
283 v6.19. We used the latest release of the XRT and UVOT Calibration Database and followed
284 standard data reduction procedures. Aperture photometry on the UVOT images was performed

285 using a circular region of radius 2.5'' centered on the afterglow position. When necessary,
286 adjacent exposures were co-added in order to increase the signal. We adopted the standard
287 photometric zero points in the *Swift* UVOT calibration database³⁰. The resulting *Swift* light
288 curves are shown in Extended Data Figure 1.

289 **RATIR Observations**

290 RATIR obtained simultaneous multi-color (*riZYJH*) imaging of GRB160625B starting at T_0+8
291 hrs and monitored the afterglow for the following 50 days until it fell below its detection
292 threshold. RATIR data were reduced and analyzed using standard astronomy algorithms.
293 Aperture photometry was performed with SExtractor³¹ and the resulting instrumental magnitudes
294 were compared to Pan-STARRS1³² in the optical and 2MASS³³ in the NIR to derive the image
295 zero points. Our final optical and infrared photometry is shown in Extended Data Figure 1.

296 **Radio observations**

297 Radio observations were carried out with the Australian Telescope Compact Array (ATCA; PI:
298 Troja) and the Jansky Very Large Array (VLA; PI: Cenko). The ATCA radio observations were
299 carried out on June 30th 2016 ($T_0+4.5$ d) at the center frequencies of 5.5, 7.5, 38 and 40 GHz, on
300 July 11th 2016 ($T_0+15.7$ d) at the center frequencies of 18, 20, 38 and 40 GHz and on July 24th
301 2016 ($T_0+28.6$ d) at the center frequencies of 8, 10, 18 and 20 GHz. For all epochs the frequency
302 bandwidth was 2 GHz and the array configuration was H75. The standard calibrator PKS 1934-
303 638 was observed to obtain the absolute flux density scale. The phase calibrators were PKS
304 2022+031 for 5.5-10 GHz observations and PKS 2059+034 for 18-40 GHz observations. The
305 data were flagged, calibrated and imaged with standard procedures in the data reduction package
306 MIRIAD³⁴. Multi Frequency Synthesis images were formed at 6.5, 7.5, 9, 19 and 39 GHz. The
307 target appeared point-like in all restored images.

308 The VLA observed the afterglow at three different epochs: 2016 June 30, July 09, and July 27. In
309 all of our observations we used J2049+1003 as the phase calibrator and 3C48 and the flux
310 calibrator. The observations were undertaken at a central frequency of 6 GHz (C-band) and 22
311 GHz (K-band) with a bandwidth of 4 GHz and 8 GHz, respectively. The data was calibrated
312 using standard tools in the CASA software and then imaged with the clean task. The source was
313 significantly detected in all three observations and in all bands. The radio afterglow light curve at
314 10 GHz is shown in Extended Data Figure 1.

315 **Spectral properties of the prompt GRB phase**

316 GRB 160625B is characterized by three distinct episodes of prompt gamma-ray emission,
317 separated by long periods of apparent quiescence (Fig. 1). A detailed spectral analysis of the first
318 two episodes (G1 and G2) is presented elsewhere¹⁹, and shows that the first event G1 is well
319 described by a thermal component with temperature $kT \approx 15$ keV, while the second burst G2 is
320 dominated by a non-thermal component peaking at energies $E_p \gtrsim 500$ keV and consistent with
321 synchrotron emission in a decaying magnetic field³⁵. Our spectral analysis focuses instead on the
322 third event (G3).

323 The time intervals for our analysis were selected based on the properties of the gamma-ray and
324 optical light curves. GBM data were retrieved from the public archive and inspected using the
325 standard RMFIT tool. The variable gamma-ray background in each energy channel was modeled
326 by a series of polynomial functions. Spectra were binned in order to have at least 1 count per
327 spectral bin and fit within XSPEC³⁶ by minimizing the modified Cash statistics. We used a Band
328 function³⁷ to model the spectra, and fixed the high-energy index to $\beta = -2.3$ when the data could
329 not constrain it. The best fit model was then extrapolated to lower energies in order to estimate
330 the contribution of the prompt component at optical frequencies. During the main gamma-ray

331 episode (G2), the observed optical emission is several orders of magnitude brighter than the
 332 extrapolation of the prompt component. In contrast, we found that the later prompt phase (G3)
 333 significantly contributes to the observed optical flux. This is rare but not unprecedented³⁸⁻⁴⁰: it
 334 has been shown that the majority of GRBs have an optical emission fainter than $R = 15.5$ mag
 335 when the gamma- ray emission is active, however a small fraction ($\approx 5\text{-}20\%$) exhibit a bright
 336 ($R \geq 14$ mag) optical counterpart during the prompt phase⁴¹.

337 As a further test we performed a joint time-resolved analysis of the optical and gamma-ray data
 338 during G3. The results are summarized in Extended Data Table 2. The derived broadband
 339 spectra are characterized by a low-energy photon index of -1.5 , consistent with fast cooling
 340 ($\nu_c < \nu_m$) synchrotron radiation. Our analysis constrains the spectral peak at $\nu_m \approx 2 \times 10^{19}$ Hz and, for
 341 typical conditions of internal dissipation models, the cooling frequency of the emitting electrons
 342 is $\nu_c \approx 5 \times 10^{12} (\epsilon_B/0.1)^{-3/2}$ Hz $\ll \nu_{\text{opt}} \ll \nu_m$, where we adopted the standard assumption that the
 343 magnetic energy is a constant fraction ϵ_B of the internal energy generated in the prompt
 344 dissipation process. Since the synchrotron self-absorption might suppress the emission at low
 345 frequencies, we consider below whether it affects the optical band. A simple estimate of the
 346 maximal flux is given by a blackbody emission with the electron temperature $k_B T \approx \gamma_e m_e c^2$,

$$347 \quad F_{\nu, BB} = 2 \pi \nu^2 (1+z)^3 \Gamma \gamma_e m_e \left(\frac{R_{\perp}}{D_L} \right)^2, \quad (1)$$

348 where $\nu \approx 5.5 \times 10^{14}$ Hz is the observed frequency, $z=1.406$ the GRB redshift, $\gamma_e \propto \nu^{1/2}$ the
 349 electron's Lorentz factor, Γ the bulk Lorentz factor, $D_L \approx 3 \times 10^{28}$ cm the luminosity distance and
 350 R_{\perp} the fireball size for the observer, which depends on the emission radius R_e as $R_{\perp} \sim R_e/\Gamma$. By
 351 imposing that the blackbody limit is larger than the observed optical flux $F_{\nu} \sim 90$ mJy, we obtain
 352 a lower limit to the emission radius³⁹:

353
$$R_{\min} \approx 4 \times 10^{14} \left(\frac{\Gamma}{200} \right)^{2/5} \left(\frac{\epsilon_B}{0.1} \right)^{1/10} \left(\frac{E_{\gamma, \text{iso}}}{10^{53} \text{ erg}} \right)^{1/10} \left(\frac{\Delta T}{300 \text{ s}} \right)^{-1/10} \text{ cm}, \quad (2)$$

354 where ΔT is the duration of the G3 burst, and $E_{\gamma, \text{iso}}$ is the isotropic equivalent gamma-ray energy
 355 released over ΔT . The radius derived in Eq. 2 is within the acceptable range for internal
 356 dissipation models, in particular those invoking the dissipation of large-scale magnetic fields^{25, 29}
 357 as suggested by our polarization measurements. For emission radii larger than R_{\min} the
 358 synchrotron self-absorption does not affect the optical emission, in agreement with our
 359 observations of a single power-law segment from optical to hard X-rays. These results lend
 360 further support to our conclusions.

361 **Origin of the Early Optical Emission**

362 One of the main features of GRB 160625B is its extremely bright optical emission during the
 363 prompt phase (Fig. 1). In the previous section we showed that, during G3, the data support a
 364 common origin for the optical and gamma-ray photons, consistent with a standard fast cooling
 365 synchrotron emission. Our analysis also showed that the same conclusion does not hold at earlier
 366 times. During the main burst (G2) the observed emission cannot be explained by a single spectral
 367 component (Fig. 3). A distinct physical origin for the optical and gamma-ray emissions is also
 368 suggested by the time lag between their light curves (Extended Data Figure 3).

369 A plausible interpretation is that the bright optical flash is powered by the reverse shock, and is
 370 unrelated to the prompt gamma-ray emission during G2. In this framework our first three
 371 polarization measurements probe the fireball ejecta at the larger reverse shock radius, and only
 372 the fourth observation includes the significant contribution of the prompt phase. This model can
 373 consistently explain the early optical and radio observations, as shown in more detail in the
 374 following sections. However, in its basic form¹⁷, the reverse shock emission cannot explain the
 375 rapid rise and double-peaked structure of the optical light curve.

376 A different possibility is that the early optical emission is produced by the same (or similar)
377 mechanisms powering the prompt gamma-ray phase, which would naturally explain the initial
378 sharp increase of the observed flux as well as its variability. One of the most popular hypotheses
379 is that the optical and gamma-ray photons are produced by two different radiation mechanisms⁴²:
380 synchrotron for the optical and synchrotron self-Compton (SSC) for the gamma-rays. This model
381 faces several problems, in particular the lack of temporal correlation between the low- and high-
382 energy light curves, and the absence of a bright second order IC component. Another possibility
383 is a two-components synchrotron radiation from internal shocks in a highly variable outflow⁴³.
384 This model predicts a weak high-energy emission and a delayed onset in the optical, consistent
385 with the observations. However, it presents other limitations, such as an excessive energy budget
386 and an unusually high variability of Lorentz factors.

387 In a different set of models the optical and gamma-ray photons come from two distinct emitting
388 zones within the flow. In the magnetic reconnection model⁴⁴ a bright quasi-thermal component,
389 emitted at the photospheric radius, peaks in the hard X-rays, while standard synchrotron
390 emission from larger radii is observed in the optical. This can explain most of the properties of
391 G2, but it does not reproduce well the observed spectral shape: the low-energy spectral slope
392 measured during this interval¹⁹ is too shallow to be accounted for by the Rayleigh-Jeans tail of
393 the thermal spectrum.

394 The properties of G2 are best explained by models in which the optical and gamma-ray photons
395 arise from synchrotron radiation at different lab times⁴⁵ or in different emitting regions. These
396 are for example late internal shocks from residual collisions⁴⁶ or free neutron decay⁴⁷. In this
397 framework the steep decay phase observed after the second optical peak could be powered by
398 delayed prompt emission from higher latitudes with respect to the observer's line of sight. This

399 case, in which all the polarization measurements probe the prompt emission mechanisms, only
400 strengthens our finding that the prompt optical emission is inherently polarized.

401 **Polarization**

402 Synchrotron radiation is inherently highly polarized. For a power-law energy distribution of the
403 emitting electrons ($dn/dE \propto E^{-p}$), the intrinsic linear polarization at low frequencies is
404 $\Pi_{\text{syn}}=9/13\sim 70\%$. If an ordered magnetic field permeates the GRB jet each emitting region
405 generates the maximum polarization Π_{syn} . However, due to relativistic kinematic effects, the
406 average polarization within $\frac{[\Gamma]}{[\text{SEP}]}$ the Γ^{-1} field of view is smaller and here we assume $\Pi_{\text{MAX}}\approx 50\%$
407 for the regime $v_c < v < v_m$.

408 Since an observer can only see a small area around the line of sight due to the relativistic
409 beaming, the magnetic field can be considered parallel within the visible area. Our measured
410 value $\Pi_{L,\text{min}}$ is related to the true degree of polarization as $\Pi_{L,\text{min}} = \Pi_L \cos 2\theta$ where θ is the angle
411 between the polarization direction and the x-axis of the reference system. For a random
412 orientation of the observer, if $\Pi_L \approx \Pi_{\text{MAX}}$ the chance to detect a polarization lower than $\Pi_{L,\text{min}} \sim 8\%$
413 is small ($\sim 10\%$). The observed values of $\Pi_{L,\text{min}}$ suggest that the magnetic field is largely distorted
414 even on small angular scales $\sim 1/\Gamma$, but not completely tangled yet.

415 As the detected optical light is a mixture of reverse shock and prompt emission, we now consider
416 whether our polarization measurements require the magnetic field to be distorted in both the
417 emitting regions. In our last polarimetric observation the prompt and reverse shock components
418 contribute roughly equally to the observed light so that $\Pi_{L,\text{min}} = (\Pi_{L,r} \cos 2\theta_r + \Pi_{L,p} \cos 2\theta_p) / 2 \sim$
419 8% where the subscripts refer to the prompt (p) and reverse shock (r) contributions. The first
420 three observations are dominated by the reverse shock component and show a low but stable
421 degree of polarization, $\Pi_{L,r} \cos 2\theta_r \approx 5\%$. By assuming that the reverse shock polarization remains

422 constant during our last polarimetric exposure, as expected in the presence of a large-scale
423 magnetic field³, we derive $\Pi_{L,p}\cos 2\theta_p \approx 11\%$, well below the maximum possible value. Since in
424 general $\theta_r \neq \theta_p$ the chance that our measurement is due to the instrumental set-up is $\leq 1\%$. Our data
425 therefore suggest that the distortion of the magnetic field configuration happens in the early
426 stages of the jet, at a radius comparable or smaller than the prompt emission radius.

427 **Broadband afterglow modeling**

428 Unless otherwise stated, all the quoted errors are 1σ . The temporal evolution of the X-ray,
429 optical and nIR afterglow is well described by simple power-law decays ($F \propto t^{-\alpha}$) with slopes
430 $\alpha_X = 1.22 \pm 0.06$, $\alpha_{opt} = 0.945 \pm 0.005$ and $\alpha_{IR} = 0.866 \pm 0.008$ until $T_0 + 14$ d, when the flux is observed
431 to rapidly decrease at all wavelengths with a temporal index $\alpha_j = 2.57 \pm 0.04$.

432 The X-ray spectrum is best fit by an absorbed power-law model with slope $\beta_X = 0.92 \pm 0.06$ and
433 only marginal (2σ) evidence for intrinsic absorption, $N_{H,i} = (1.6 \pm 0.8) \times 10^{21} \text{ cm}^{-2}$, in addition to
434 the galactic value $N_H = 9.6 \times 10^{20} \text{ cm}^{-2}$. A power-law fit performed on the optical/nIR data yields
435 negligible intrinsic extinction and a slope $\beta_{OIR} = 0.50 \pm 0.05$ at $T_0 + 8$ hrs, which progressively
436 softens to 0.8 ± 0.2 at $T_0 + 10$ d. The low intrinsic extinction ($E_{B-V} < 0.06$, 95% confidence level)
437 shows that dust scattering has a negligible effect⁴⁸ ($< 0.5\%$) on our measurements of polarization.

438 Within the external shock model, the difference in temporal and spectral indices indicates that
439 the X-ray and optical/IR emissions belong to two different synchrotron segments. A comparison
440 with the standard closure relations shows that the observed values are consistent with the regime
441 $\nu_m < \nu_{opt} < \nu_c < \nu_X$ for $p \approx 2.2$. The color change of the optical/IR afterglow suggests that the
442 cooling break decreases and progressively approaches the optical range. This feature is
443 distinctive of a forward shock expanding into a medium with a homogeneous density profile⁴⁹.
444 However, the measured radio flux and spectral slope cannot be explained by the same

445 mechanism, and require an additional component of emission, likely originated by a strong
 446 reverse shock re-heating the fireball ejecta as it propagates backward through the jet. This is also
 447 consistent with our observations of a bright optical flash at early times¹⁷. In order to test this
 448 hypothesis, we created seven different spectral energy distributions (SEDs) at different times,
 449 ranging from $T_0+0.4$ d to T_0+30 d, and modeled the broadband afterglow and its temporal
 450 evolution with a forward shock + reverse shock (FS + RS) model^{17,49}. The best fit afterglow
 451 parameters are an isotropic-equivalent kinetic energy $\log E_{K,iso} = 54.3^{+0.17}_{-0.5}$, a low circumburst
 452 density $\log n = -4.0^{+1.7}_{-1.1}$, and microphysical parameters $\log \epsilon_e = -1.0^{+0.5}_{-1.0}$ and $\log \epsilon_B = -2.0 \pm 1.0$.
 453 These results are consistent with the trend of a low density environment, and high radiative
 454 efficiency observed in other bright bursts^{50,51}. Our data and best fit model are shown in Extended
 455 Data Figure 4.

456 In this framework, the achromatic temporal break at T_0+14 d is the result of the outflow
 457 geometry, collimated into a conical jet with a narrow opening angle $\theta_j = 2.4^{+1.6}_{-0.7}$ deg. This
 458 lessens the $\left[\frac{L}{4\pi d^2}\right]_{SEP}$ energy budget by a factor θ_j^2 and the resulting collimation corrected energy release
 459 $\sim 6 \times 10^{51}$ erg is within the range of other GRBs. The extreme luminosity of GRB160625B can be
 460 therefore explained, at least in part, by its outflow geometry as we are viewing the GRB down
 461 the core of a very narrow jet.

462 The large flux ratio between the RS and FS at peak, $f_{RS}/f_{FS} > 5 \times 10^3$, implies a high magnetization
 463 parameter^{52,53} $R_B \approx \epsilon_{B,RS} / \epsilon_{B,FS} > 100 (\Gamma/500)^2 \gg 1$, and shows that the magnetic energy density
 464 within the fireball is larger than in the forward shock. From our broadband modeling we derived
 465 a best fit value of $\epsilon_{B,FS} \approx 0.01$ with a 1 dex uncertainty, which allows us to estimate the ejecta
 466 magnetic content in the range $\sigma \geq 0.1$, where solutions with $\sigma > 1$ would suppress the reverse shock
 467 emission and are therefore disfavored.

468

469 **Additional References**

- 470 30. Breeveld, A. A., Landsman, W., Holland, S. T., et al. An Updated Ultraviolet Calibration for
471 the *Swift*/UVOT, *American Institute of Physics Conference Series* **1358**, 373-376 [SEP](2011)
- 472 31. Bertin, E., & Arnouts, S. SExtractor: Software for source extraction. *Astron. Astrophys.*
473 *Supp.* **117**, 393-404 [SEP](1996)
- 474 32. Chambers, K. C., Magnier, E. A., Metcalfe, N., et al. The Pan-STARRS1 Surveys. Preprint
475 available at <https://arxiv.org/abs/1612.05560> [SEP](2016)
- 476 33. Skrutskie, M. F., Cutri, R. M., Stiening, R., et al. The Two Micron All Sky Survey (2MASS).
477 *Astron. J.* **131**, 1163-1183 [SEP](2006)
- 478 34. Sault, R. J., Teuben, P. J., & Wright, M. C. H. A Retrospective View of MIRIAD.
479 *Astronomical Data Analysis Software and Systems IV* **77**, 433-436 [SEP](1995)
- 480 35. Uhm, Z. L., & Zhang, B. Fast-cooling synchrotron radiation in a decaying magnetic field and
481 γ -ray burst emission mechanism. *Nature Physics* **10**, 351-356 [SEP](2014)
- 482 36. Arnaud, K. A. XSPEC: The First Ten Years. *Astronomical Data Analysis Software and*
483 *Systems V* **101**, 17-20 [SEP](1996)
- 484 37. Band, D., Matteson, J., Ford, L., et al. BATSE observations of gamma-ray burst spectra. I -
485 Spectral diversity. *Astrophys. J.* **413**, 281-292 [SEP](1993)
- 486 38. Vestrand, W. T., Woźniak, P. R., Wren, J. A., et al. A link between prompt optical and
487 prompt γ -ray emission in γ -ray bursts. *Nature* **435**, 178-180 [SEP](2005)
- 488 39. Shen, R.-F., & Zhang, B. Prompt optical emission and synchrotron self-absorption
489 constraints on emission site of GRBs. *Mon. Not. R. Astron. Soc.* **398**, 1936-1950 [SEP](2009)

- 490 40. Gendre, B., Atteia, J. L., Boër, M., et al. GRB 110205A: Anatomy of a Long Gamma- Ray
491 Burst. *Astrophys. J.* **748**, 59 [SEP](2012)
- 492 41. Klotz, A., Boër, M., Atteia, J. L., & Gendre, B. Early Optical Observations of Gamma-Ray
493 Bursts by the TAROT Telescopes: Period 2001-2008. *Astron. J.* **137**, 4100-4108 [SEP](2009)
- 494 42. Kumar, P., & Panaitescu, A. What did we learn from gamma-ray burst 080319B? *Mon. Not.*
495 *R. Astron. Soc.* **391**, L19-L23 [SEP](2008)
- 496 43. Yu, Y. W., Wang, X. Y., & Dai, Z. G. Optical and γ -ray Emissions from Internal Forward-
497 Reverse Shocks: Application to GRB 080319B? *Astrophys. J.* **692**, 1662-1668 [SEP](2009)
- 498 44. Giannios, D. Prompt GRB emission from gradual energy dissipation. *Astron. Astrophys.* **480**,
499 305-312 [SEP](2008)
- 500 45. Wei, D. M. The GRB early optical flashes from internal shocks: application to
501 [SEP]GRB990123, GRB041219a and GRB060111b. *Mon. Not. R. Astron. Soc.* **374**, 525-529
502 [SEP](2007)
- 503 46. Li, Z., & Waxman, E. Prompt Optical Emission from Residual Collisions in Gamma- [SEP]Ray
504 Burst Outflows. *Astrophys. J.* **674**, L65-L68 [SEP](2008)
- 505 47. Fan, Y. Z., Zhang, B., & Wei, D. M. Early Optical-Infrared Emission from GRB 041219a:
506 Neutron-rich Internal Shocks and a Mildly Magnetized External Reverse Shock. *Astrophys.*
507 *J.* **628**, L25-L28 [SEP](2005)
- 508 48. Serkowski, K., Matheson, D. S. & Ford, V. L. Wavelength dependence of interstellar
509 polarisation and ratio of total to selective extinction. *Astrophys. J.* **196**, 261 [SEP](1975)
- 510 49. Granot, J., & Sari, R. The Shape of Spectral Breaks in Gamma-Ray Burst Afterglows.
511 *Astrophys. J.* **568**, 820-829 [SEP](2002)

- 512 50. Cenko, S. B., Frail, D. A., Harrison, F. A., et al. Afterglow Observations of Fermi Large
513 Area Telescope Gamma-ray Bursts and the Emerging Class of Hyper-energetic Events.
514 *Astrophys. J.* **732**, 29 [SEP](2011)
- 515 51. Ackermann, M., Ajello, M., Asano, K., et al. Multiwavelength Observations of GRB
516 110731A: GeV Emission from Onset to Afterglow. *Astrophys. J.* **763**, 71 [SEP](2013)
- 517 52. Zhang, B., Kobayashi, S., & Mészáros, P. Gamma-Ray Burst Early Optical Afterglows:
518 Implications for the Initial Lorentz Factor and the Central Engine. *Astrophys. J.* **595**, 950-954
519 [SEP](2003)
- 520 53. Zhang, B., & Kobayashi, S. Gamma-Ray Burst Early Afterglows: Reverse Shock Emission
521 from an Arbitrarily Magnetized Ejecta. *Astrophys. J.* **628**, 315-334 [SEP](2005)

522

523

524

525 **Data availability:** All relevant data are available from the corresponding author upon reasonable
526 request. Data presented in Figure 1, and Extended Data Figure 1 are included with the
527 manuscript. *Swift* XRT data are available at http://www.swift.ac.uk/xrt_products/

528

529

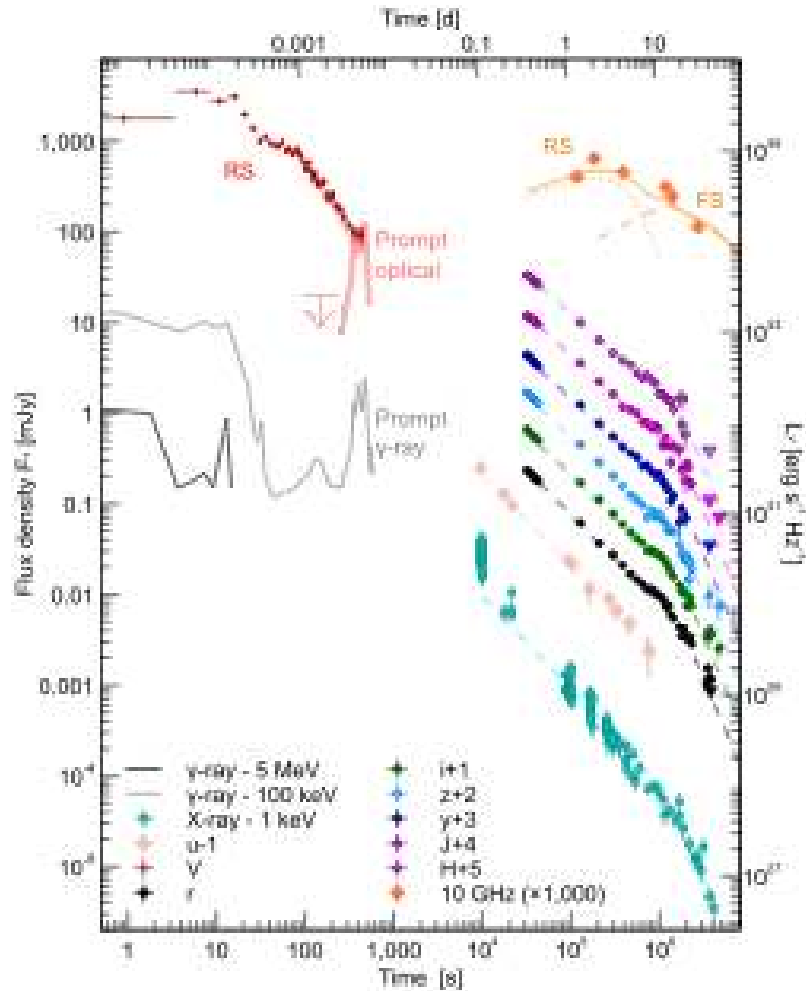
530

531

532

533

534

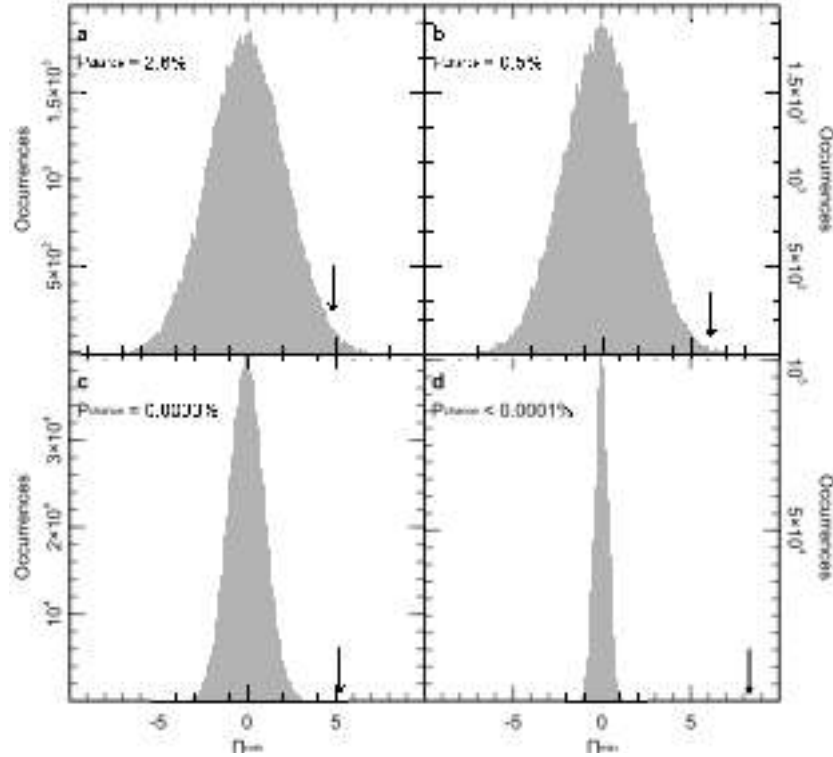


535

536 **Extended Data Figure 1: Multi-wavelength light curves of GRB160625B and its afterglow.**

537 Different emission components shape the temporal evolution of GRB160625B. On timescales of
 538 seconds to minutes after the explosion, we observe bright prompt (solid lines) and reverse shock
 539 (dotted lines) components. On timescales of hours to weeks after the burst, emission from the
 540 forward shock (dashed lines) becomes the dominant component from X-rays down to radio
 541 energies. After ≈ 14 d, the afterglow emission rapidly falls off at all wavelengths. This
 542 phenomenon, known as jet-break, is caused by the beamed geometry of the outflow. Error bars
 543 are 1σ , and upper limits are 3σ . Times are referred to the LAT trigger time T_0 .

544



545

546 **Extended Data Figure 2: Results of the Monte Carlo simulations.**

547 For each of the four polarization epochs we simulated and examined a large number of datasets
 548 with similar photometric properties and no intrinsic afterglow polarization. **a** Results of 10^5
 549 simulations for the first epoch (95 s – 115 s) **b** Same as **a** but for the second epoch (144 s - 174 s)
 550 **c** Results of 10^6 simulations for the third epoch (186 s - 226 s) **d** Same as **c** but for the fourth
 551 epoch (300 s - 360 s). The observed value is shown by a vertical arrow. The probability of
 552 obtaining by chance a polarization measurement as high as the observed value is also reported.

553

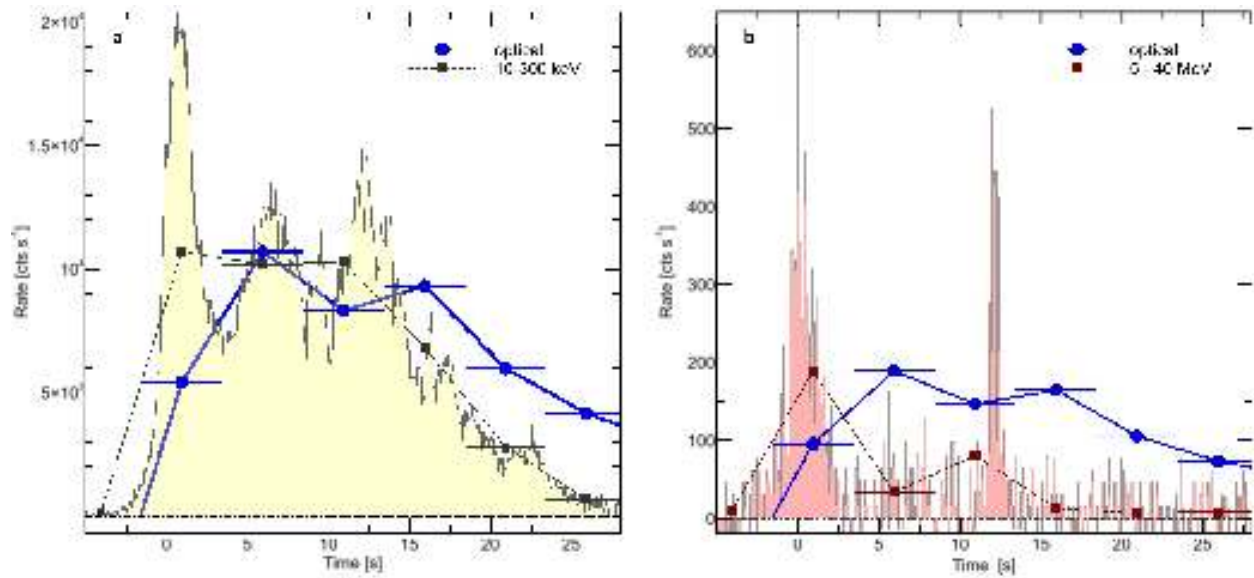
554

555

556

557

558



559

560 **Extended Data Figure 3: A comparison of the early gamma-ray and optical emission**
 561 **measured for GRB 160625B**

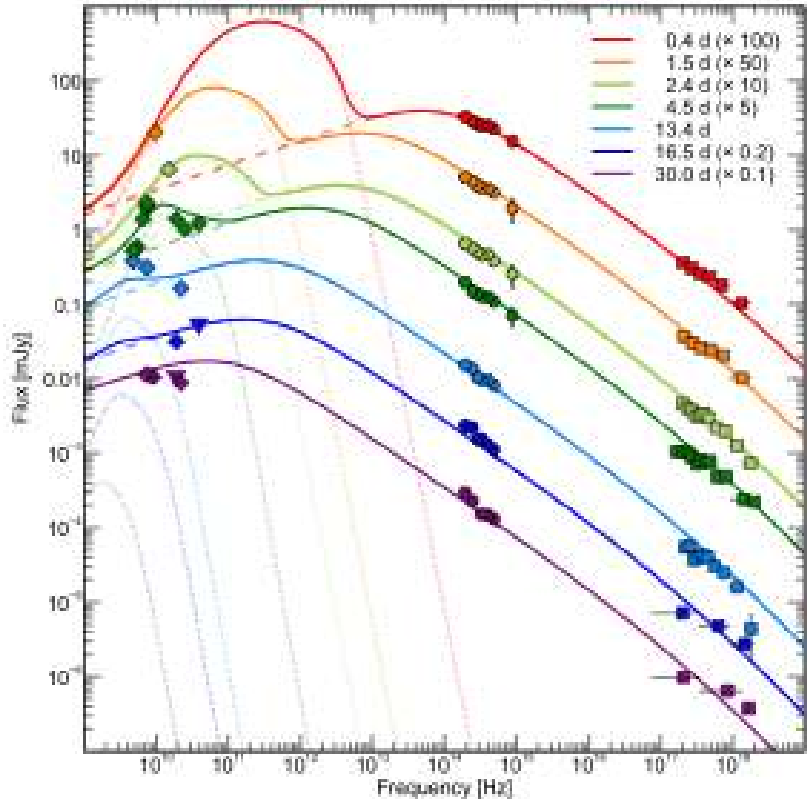
562 **a** Gamma-ray light curves in the soft (50–300 keV) energy band. **b** Gamma-ray light curves in
 563 the hard (5–40 MeV) energy band. Optical data (blue circles) are arbitrarily rescaled. The
 564 squared points show the gamma-ray light curves rebinned by adopting the same time intervals of
 565 the optical observations. Times are referred to the LAT trigger time T_0 .

566

567

568

569



570

571 **Extended Data Figure 4: Afterglow spectral energy distributions of GRB 160625B.**

572 The afterglow evolution can be described by the combination of forward shock (dashed lines)
 573 and reverse shock (dotted lines) emission. The best fit model is shown by the solid lines. The
 574 peak flux of the forward shock component is ≈ 0.4 mJy, significantly lower than the optical flux
 575 measured at $T < T_0 + 350$ s. This shows that the forward shock emission is negligible during the
 576 prompt phase. Error bars are 1σ , and upper limits are 3σ .

577

578

579

580

581

582

583 **Extended Data Table 1: Polarimetry Results.**

Time since T_0 [mid; s]	Exposure time [s]	$\Pi_{L,\min}$ [%]	Error [1 σ ; %]
105	20	4.8	1.7
159	30	6.1	1.4
206	40	5.2	0.6
330	60	8.3	0.5

584

585

586

587 **Extended Data Table 2: Spectral properties of the prompt emission for GRB 160625B.**

Time interval [s]	Detectors	α	β	E_p [keV]	Flux (10-10 ⁴ keV) [10 ⁻⁷ erg cm ⁻² s ⁻¹]	W-Stat	dof
0.10-19.10 (G2)	Nal ₇ , Nal ₆ , BGO ₁	-0.733±0.010	-2.50±0.04	680±20	429±5	250	204
337-607 (G3)	Nal ₆ , BGO ₁	-1.52±0.04	2.3	140 ⁺⁴⁰ ₋₃₀	2.30±0.10	211	77
Time-Resolved Analysis							
334-359	Nal ₆ , BGO ₁	-1.53±0.02	2.3	>210	3.2±0.5	60	74
359-384	Nal ₆ , BGO ₁	-1.55±0.03	2.3	>180	2.4±0.7	58	74
384-414	Nal ₆ , BGO ₁	-1.49±0.02	2.3	>210	3.9±0.7	67	72
414-464	Nal ₆ , BGO ₁	-1.53±0.04	2.3	270±80	3.2±0.3	68	73
464-499	Nal ₆ , BGO ₁	-1.45±0.03	2.3	130±15	4.9±0.3	62	81

588

589 The GRB prompt emission can be described by a smoothly broken power-law³⁷ with low-energy
590 index α , high-energy index β , and peak energy E_p . Errors are 1 σ , lower limits are at 95%
591 confidence level. Given the high statistical quality of the G2 spectrum a 5% systematic error was
592 added to the fit.

593

594

595

596

597

598

599 **Acknowledgements** ET thank L. Piro and K. Murase for comments. We thank the RATIR
600 project team and the staff of the Observatorio Astronómico Nacional on Sierra San Pedro Mártir,
601 and acknowledge the contribution of Leonid Georgiev and Joshua S. Bloom to its development.
602 RATIR is a collaboration between the University of California, the Universidad Nacional
603 Autónoma de México, NASA Goddard Space Flight Center, and Arizona State University,
604 benefiting from the loan of an H2RG detector and hardware and software support from Teledyne
605 Scientific and Imaging. RATIR, the automation of the Harold L. Johnson Telescope of the
606 Observatorio Astronómico Nacional on Sierra San Pedro Mártir, and the operation of both are
607 funded through NASA grants NNX09AH71G, NNX09AT02G, NNX10AI27G, and
608 NNX12AE66G, CONACyT grants INFR-2009-01-122785 and CB-2008-101958, UNAM
609 PAPIIT grant IN113810, and UC MEXUS-CONACyT grant CN 09-283. The MASTER project
610 is supported in part by the Development Program of Lomonosov Moscow State University,
611 Moscow Union OPTICA, Russian Science Foundation 16-12-00085. This work was supported in
612 part by NASA Fermi grants NNH15ZDA001N and NNH16ZDA001N. This work made use of
613 data supplied by the UK Swift Science Data Centre at the University of Leicester, funded by the
614 UK Space Agency.

615

616 **Author Contributions** ET, CGM, and SK composed the text based on inputs from all the co-
617 authors. MASTER data were provided, reduced and analyzed by VML, ESG and NVT. RATIR
618 observations were obtained, reduced and analyzed by NRB, ET, AMW, AK, WHL, and VT.
619 FEM processed and analyzed the *Swift*/UVOT data. ET, RR and MW obtained, processed and
620 analyzed the ATCA observations. VLA observations were obtained, processed and analyzed by

621 SBC, AF, AH. All authors assisted in obtaining parts of the presented dataset, discussed the
622 results or commented on the manuscript.

623

624 **Competing financial interests** The authors declare no competing financial interests.

625

626 **Correspondence** Correspondence and requests for materials should be addressed to E. Troja

627 (eleonora.troja@nasa.gov).

628